Supplement of Atmos. Chem. Phys., 25, 13651–13664, 2025
https://doi.org/10.5194/acp-25-13651-2025-supplement

Atmospheric Chemistry and Physics
Open Access
EGU

Supplement of

Role of in situ-excited planetary waves in polar vortex splitting during the 2002 Southern Hemisphere sudden stratospheric warming event

Ji-Hee Yoo and Hye-Yeong Chun

Correspondence to: Hye-Yeong Chun (chunhy@yonsei.ac.kr)

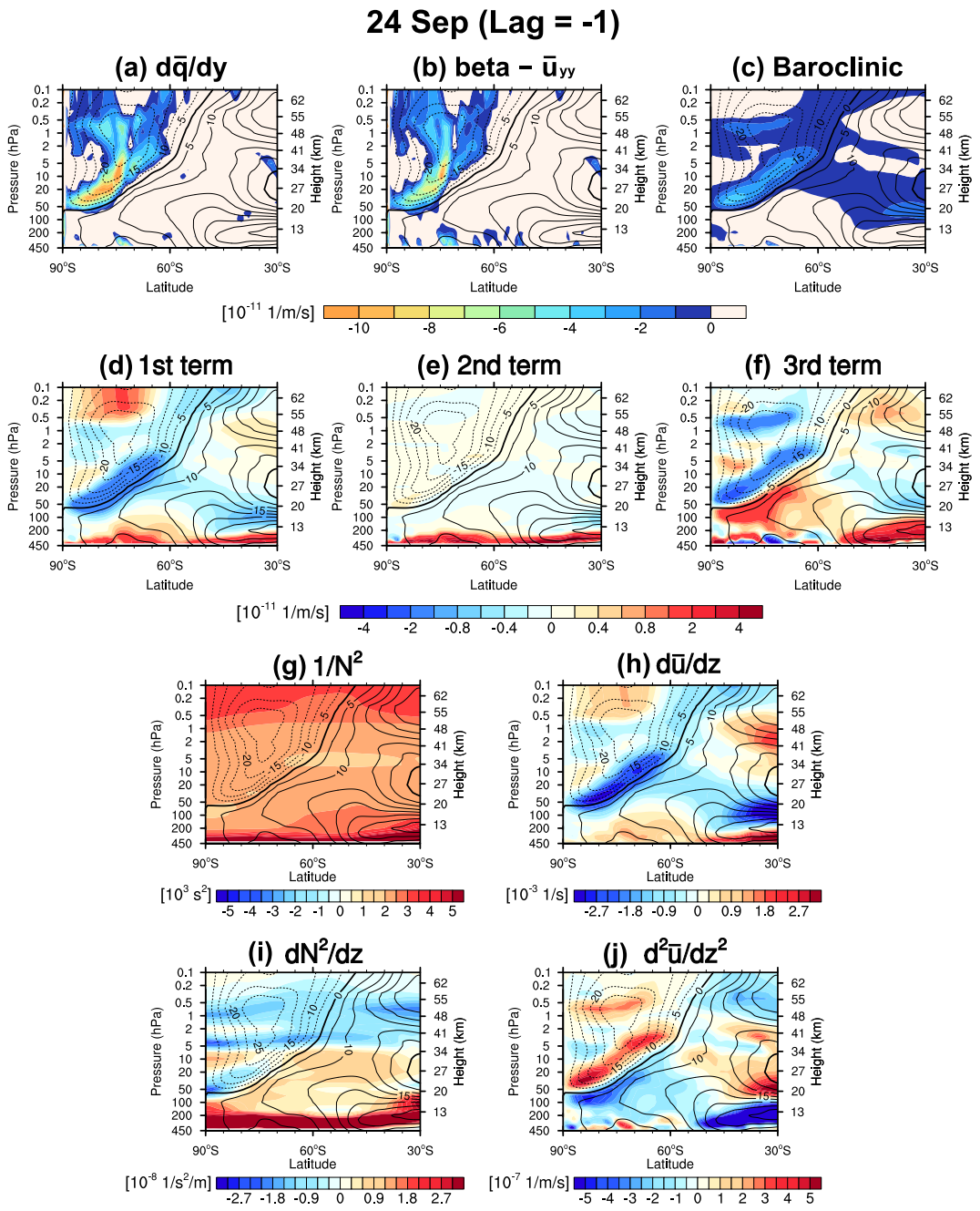

Figure S1. Latitude–height cross sections of (a–c) $\bar{q}_y$, the sum of first two terms (the meridional gradient of f and barotropic term), and the third term (baroclinic term) on the right-hand side of Eq. (S1) and (d–f) the three terms on the right-hand side of Eq. (S2) divided by f^2, (d) the inverse squared Brunt–Väisälä frequency $1/N^2$, the vertical shear of zonal wind $\bar{u}_z$, the vertical gradient of Brunt–Väisälä frequency dN^2/dz, and the vertical curvature of zonal wind $\bar{u}_{zz}$, on 24 September 2002. The black contours represent the zonal-mean zonal winds. The solid, dashed, and thick solid lines denote positive, negative, and zero wind, respectively.

Text S1.

To better understand the mechanism by which the strengthening easterlies induce instability, we conduct a detailed examination of the individual subterms contributing to $\bar{q}_y$:

$$\bar{q}_y = \frac{\partial \bar{q}}{a\partial\phi} = \frac{2\Omega\, cos\,\phi}{a} - \frac{1}{a^2}\frac{\partial}{\partial\phi}\left[\frac{1}{cos\,\phi}\frac{\partial(\bar{u}\, cos\,\phi)}{\partial\phi}\right] - \frac{1}{\rho_0}\frac{\partial}{\partial z}\left(\rho_0 \frac{f^2}{N^2}\frac{\partial \bar{u}}{\partial z}\right). \quad \text{(S1)}$$

Figure S1a–c present the latitude–height cross sections of $\bar{q}_y$, the sum of first two terms (the meridional gradient of f and barotropic term), and the third term (baroclinic term) on the right-hand side of Eq. (S1) on 24 September—a representative case during the vortex destabilization period (22–25 September). The strengthening easterlies induce a positive curvature of zonal wind (barotropic term) along their core, which dominates over the meridional gradient of f, leading to a negative sum of the two terms (Fig. S1b). Simultaneously, the baroclinic term becomes negative both below (50–5 hPa) and above (2–0.5 hPa) the easterly jet core in the polar stratosphere (60°–90°S, Fig. S1c).

To clarify the mechanisms driving the negative baroclinic term, we further expand it as follows (Yoo et al. 2023):

$$-\frac{1}{\rho_0}\left(\rho_0 \frac{f^2}{N^2}\bar{u}_z\right)_z = f^2\left[\frac{1}{H}\frac{1}{N^2}\bar{u}_z + \frac{1}{N^4}\frac{dN^2}{dz}\bar{u}_z - \frac{1}{N^2}\bar{u}_{zz}\right]. \quad \text{(S2)}$$

Figure S1d–f display the first, second, and third subterms of Eq. (S2), respectively, divided by f^2. Both the first (Fig. S1d) and third terms (Fig. S1f) contribute to the negative baroclinic term within the developing easterlies over the polar stratosphere (Fig. S1c). Figure S1g–j present the distributions of four variables involved in the three subterms of Eq. (S2): the inverse squared Brunt–Väisälä frequency ($1/N^2$), the vertical shear of zonal wind ($\bar{u}_z$), the vertical gradient of Brunt–Väisälä frequency (dN^2/dz), and the vertical curvature of zonal wind ($\bar{u}_{zz}$), respectively. Under positive $1/N^2$ (Fig. S1g), the first subterm (Fig. S1d) becomes negative due to the easterlies descending from the lower mesosphere, which generate negative vertical shear ($\bar{u}_z$) along and below the jet core (Fig. S1h). The third subterm (Fig. S1f), showing distinct negative values above (2–0.5 hPa) and below (50–5 hPa) the easterly core, is attributed to strong positive vertical curvature ($\bar{u}_{zz}$) in these regions with positive $1/N^2$ (Fig. S1g and j).

In summary, the negative baroclinic term arises primarily from two processes: negative $\bar{u}_z$ beneath and near the easterly jet core, and enhanced positive $\bar{u}_{zz}$ both above and below the jet core.

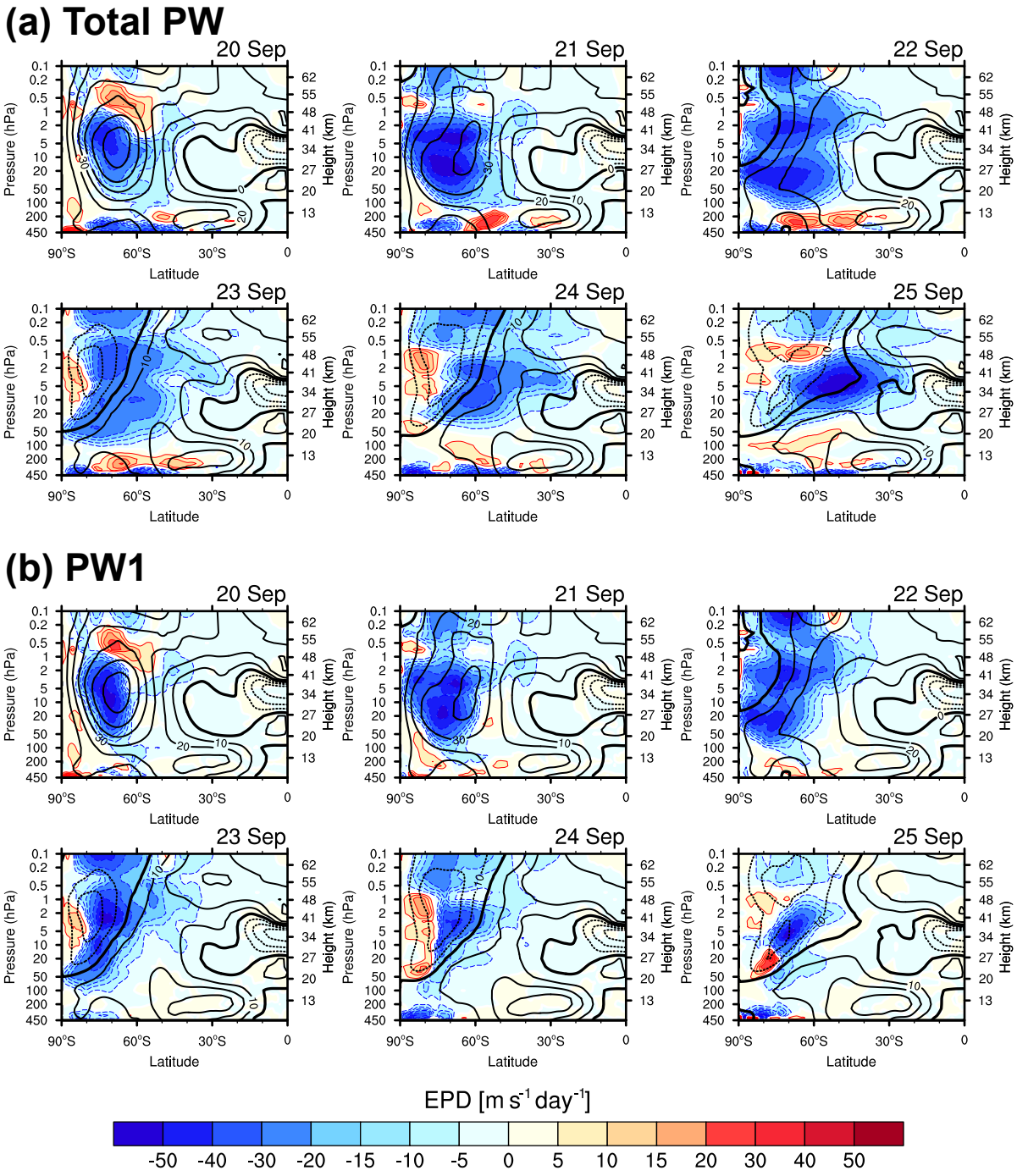

Figure S2. Latitude–height cross sections of EP-flux (vectors) overlaid on EPFD (shading) for (a) total PWs and (b) PW1 from 20 to 25 September 2002. EP-flux vectors are scaled following the same method as in Fig. 3 in the original manuscript. Black contours indicate zonal-mean zonal wind, with the contour specifications identical to those in Fig. 3.

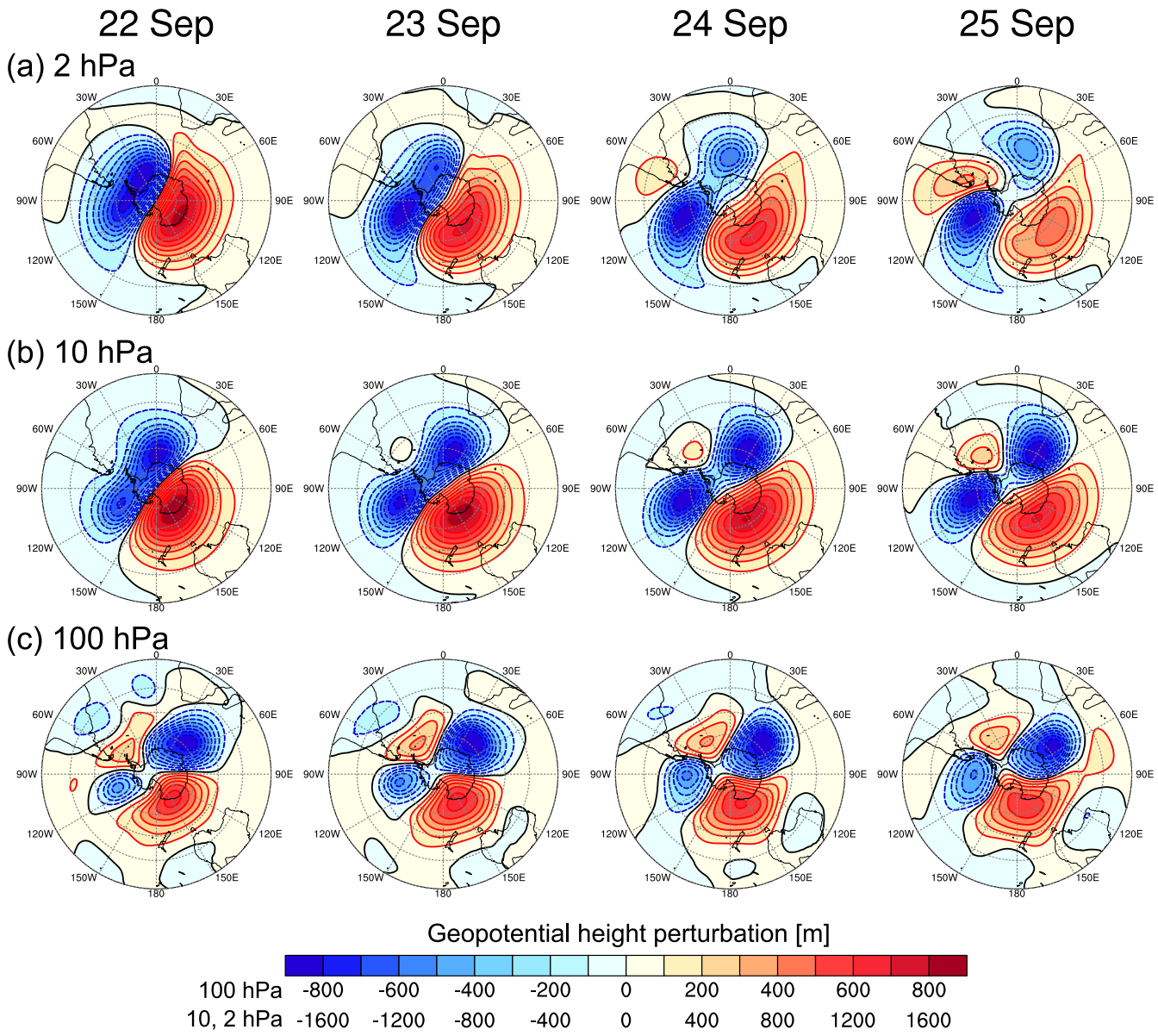

47

48 **Figure S3.** Polar stereographic series of GHP at (a) 2 hPa, (b) 10 hPa, and (c) 100 hPa from 22 to 25 September 2002.

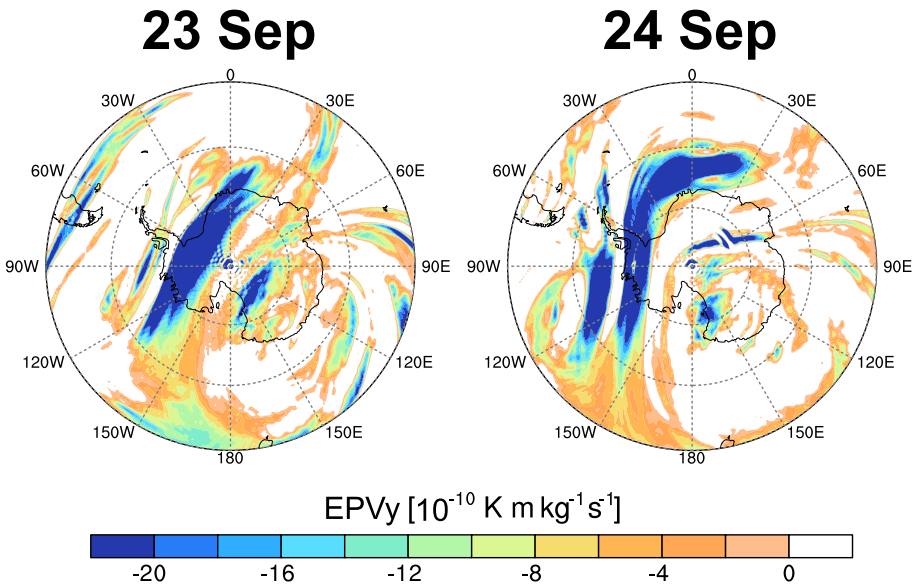

Figure S4. Meridional gradient of Ertel's potential vorticity at the 1500 K isentropic surface in 23–24 September 2002.

Table S1: Wave-2-type SSW events identified from Modern-Era Retrospective analysis for Research and Applications (version 2) data in the Northern Hemisphere (NH) from 1980 to 2023. SSW events are classified using the criterion established by Charlton and Polvani (2007), while wave-2-type SSW events are identified following the method of Ryoo and Chun (2005).

	Onset date	**In situ planetary wave 2 generation signal**
1	1 Jan 1985	N
2	8 Dec 1987	**Y**
3	14 Mar 1988	N
4	21 Feb 1989	N
5	15 Dec 1998	**Y**
6	11 Feb 2001	**Y**
7	18 Jan 2003	**Y**
8	24 Feb 2007	**Y**
9	24 Jan 2009	N
10	6 Jan 2013	**Y**
11	12 Feb 2018	N

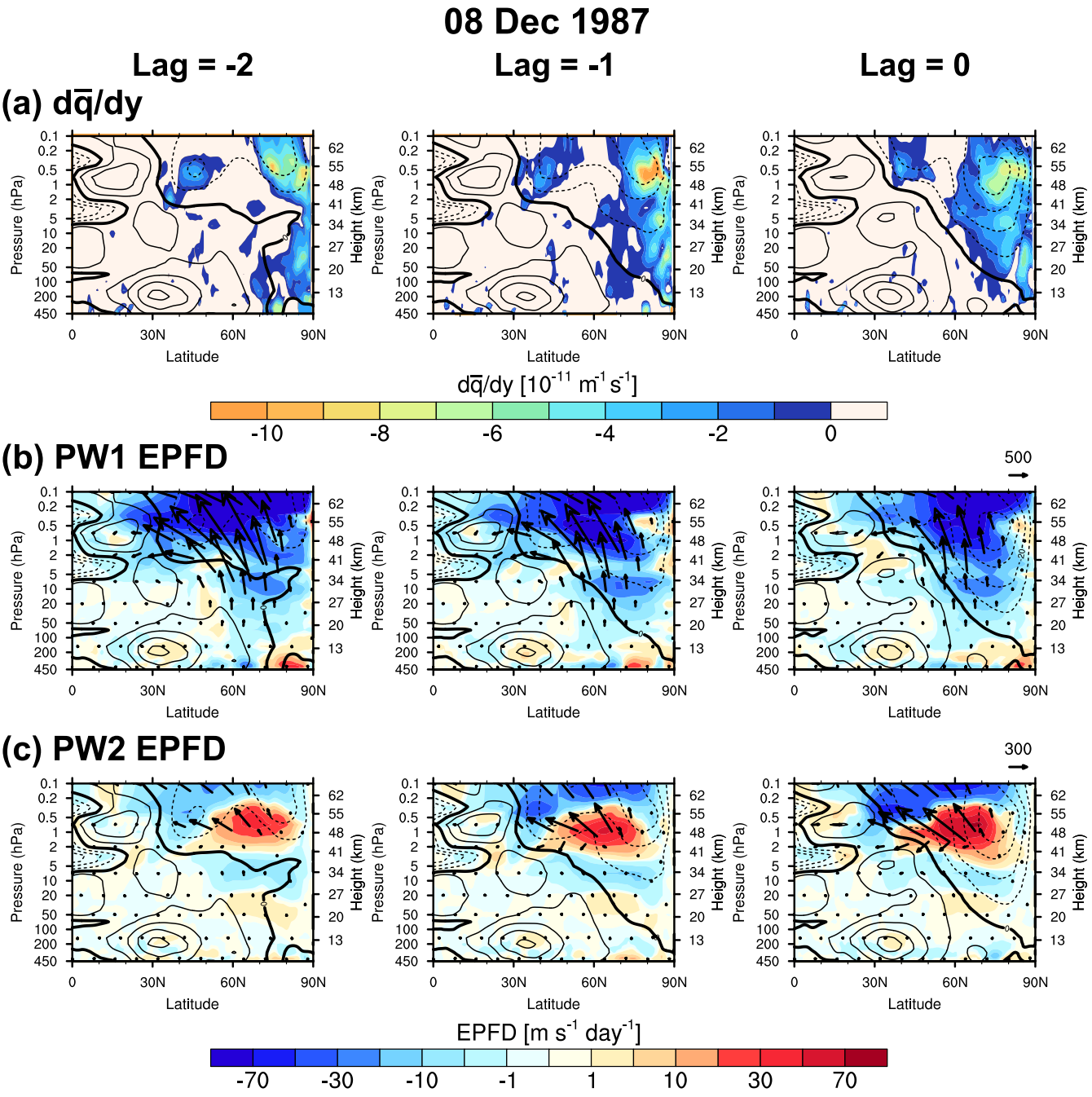

59 **Figure S5:** Latitude–height cross sections of (a) negative $\bar{q}_y$ (shading) and EP-flux (vectors) overlaid with EPFD (shading)
60 for (b) PW1 and (c) PW2 from Lag = –2 to Lag = 0 during the SSW event on 8 December 1987 among six NH SSW cases
61 showing in situ PW2 generation in Table 1. Black contours indicate zonal-mean zonal wind with solid, dashed, and thick
62 solid lines indicating positive, negative, and zero wind, respectively. EP-flux vectors are scaled following the same method
63 as in Fig. 3 in the original manuscript [unit: $m^2\ s^{-2}$].

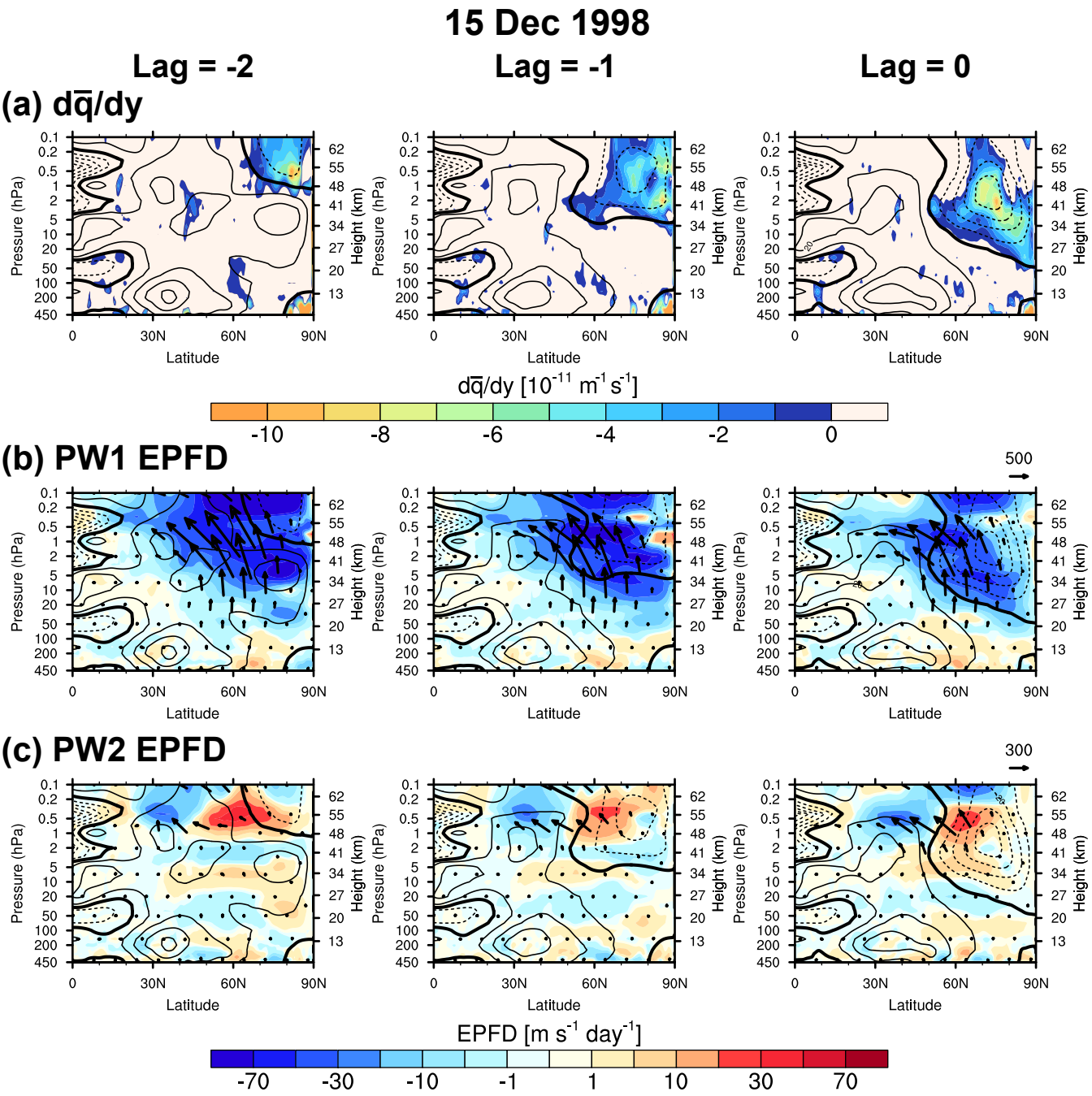

Figure S6. Same as Figure S5, but for 15 December 1998.

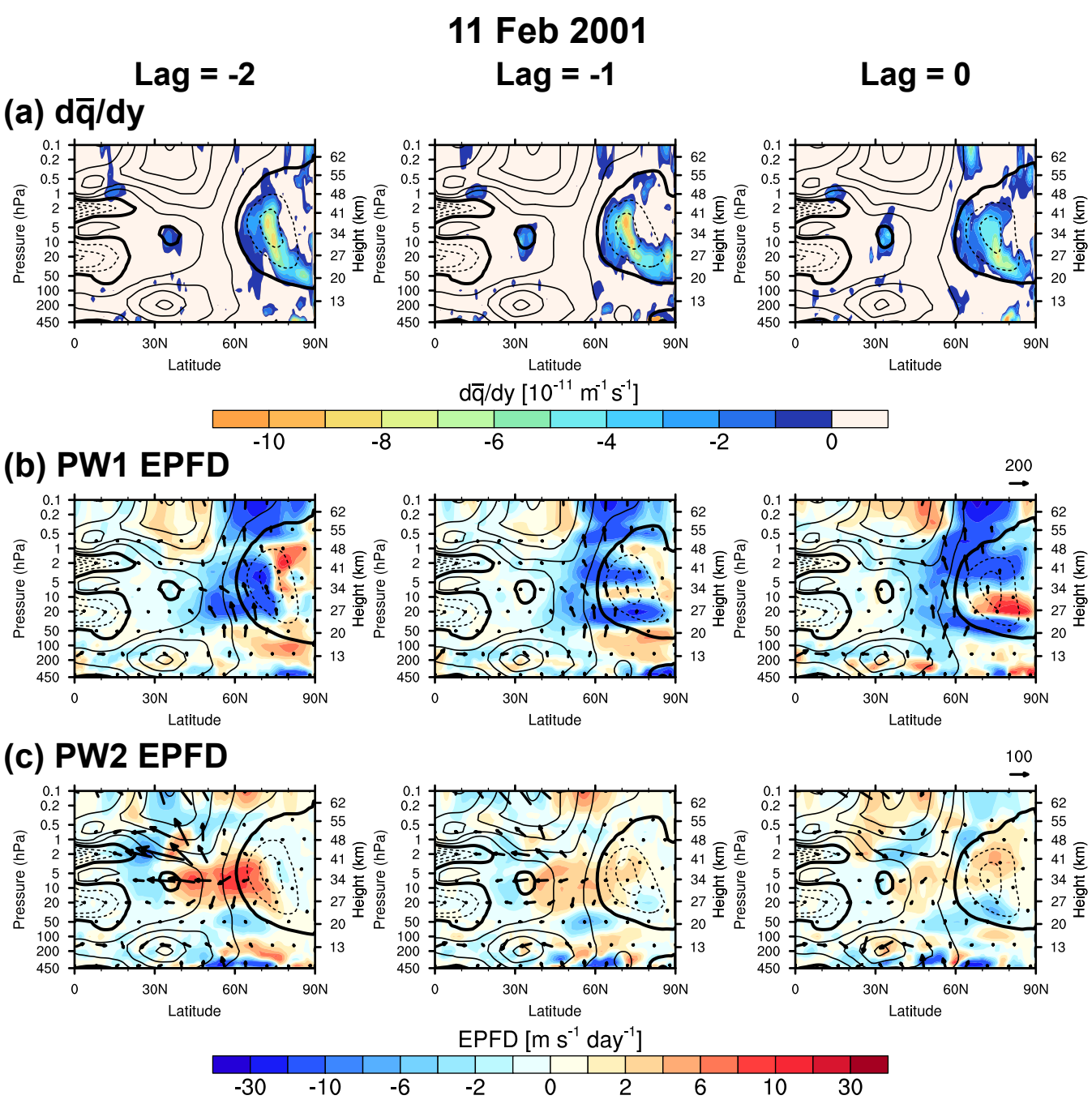

Figure S7. Same as Figure S5, but for 11 February 2001.

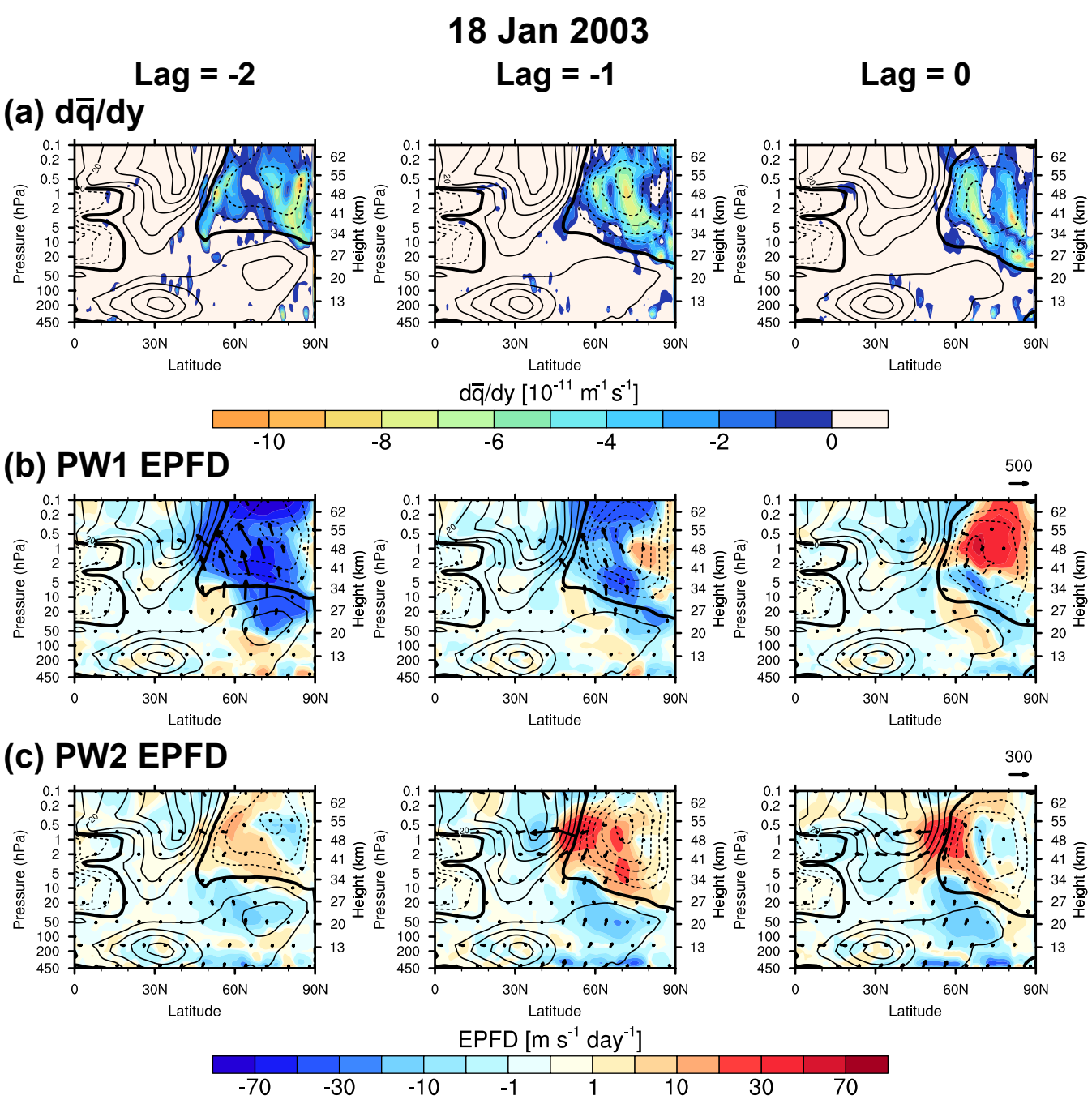

Figure S8. Same as Figure S5, but for 18 January 2003.

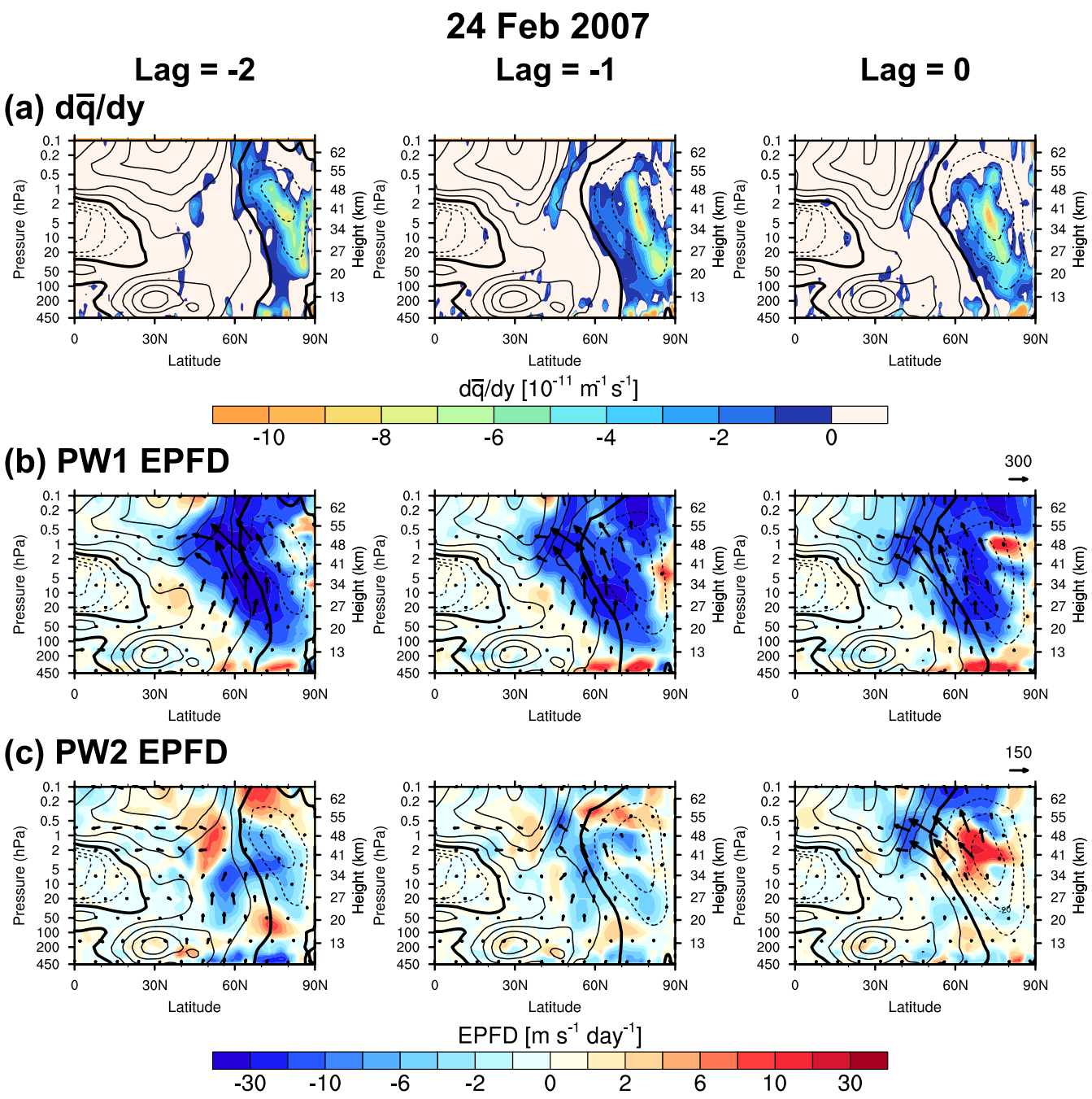

Figure S9. Same as Figure S5, but for 24 February 2007.

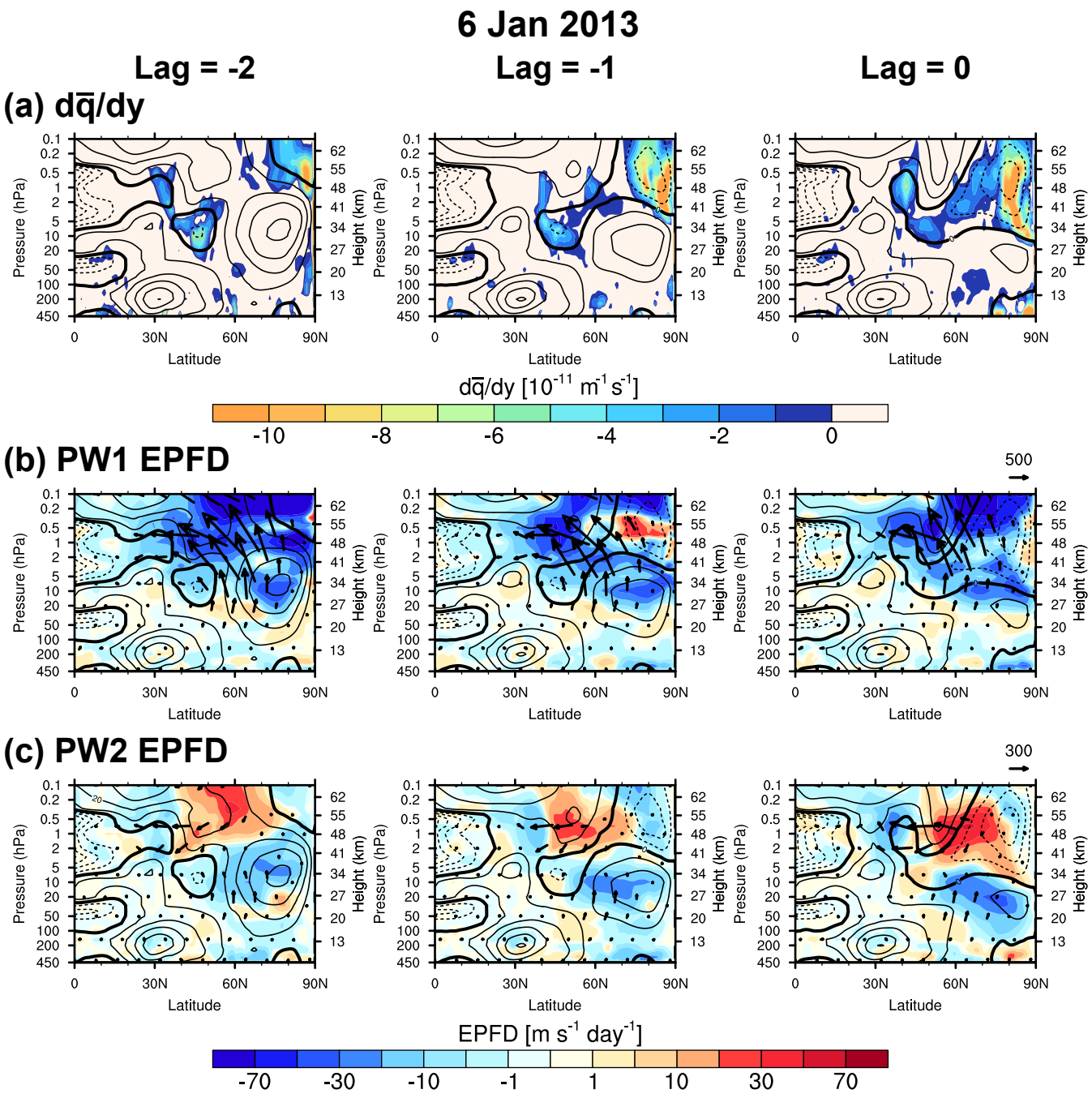

Figure S10. Same as Figure S5, but for 6 January 2013.

Text S2.

Given the limited reanalysis reliability in the upper stratosphere and lower mesosphere due to sparse observations, we conduct the major analysis in this study by using two additional reanalysis datasets for comparison to provide support the validity of our results: the fifth generation of the European Centre for Medium-Range Weather Forecasts (ECMWF) Reanalysis re-run for 2000–2006 (ERA5.1, Simmons et al., 2020) and the Japanese Reanalysis for Three Quarters of a Century (JRA-3Q; Kosaka et al., 2024).

ERA5.1 is provided on 137 hybrid sigma–pressure levels up to 0.01 hPa (~80 km), with a horizontal resolution of 0.25° and 1-hourly temporal resolution. JRA-3Q is provided on a Gaussian grid with a latitude resolution of approximately 0.56° and 43 vertical levels spanning from 1000 to 0.1 hPa, with 6-hourly resolution. All results presented are based on daily averages (Figures S11–S13).

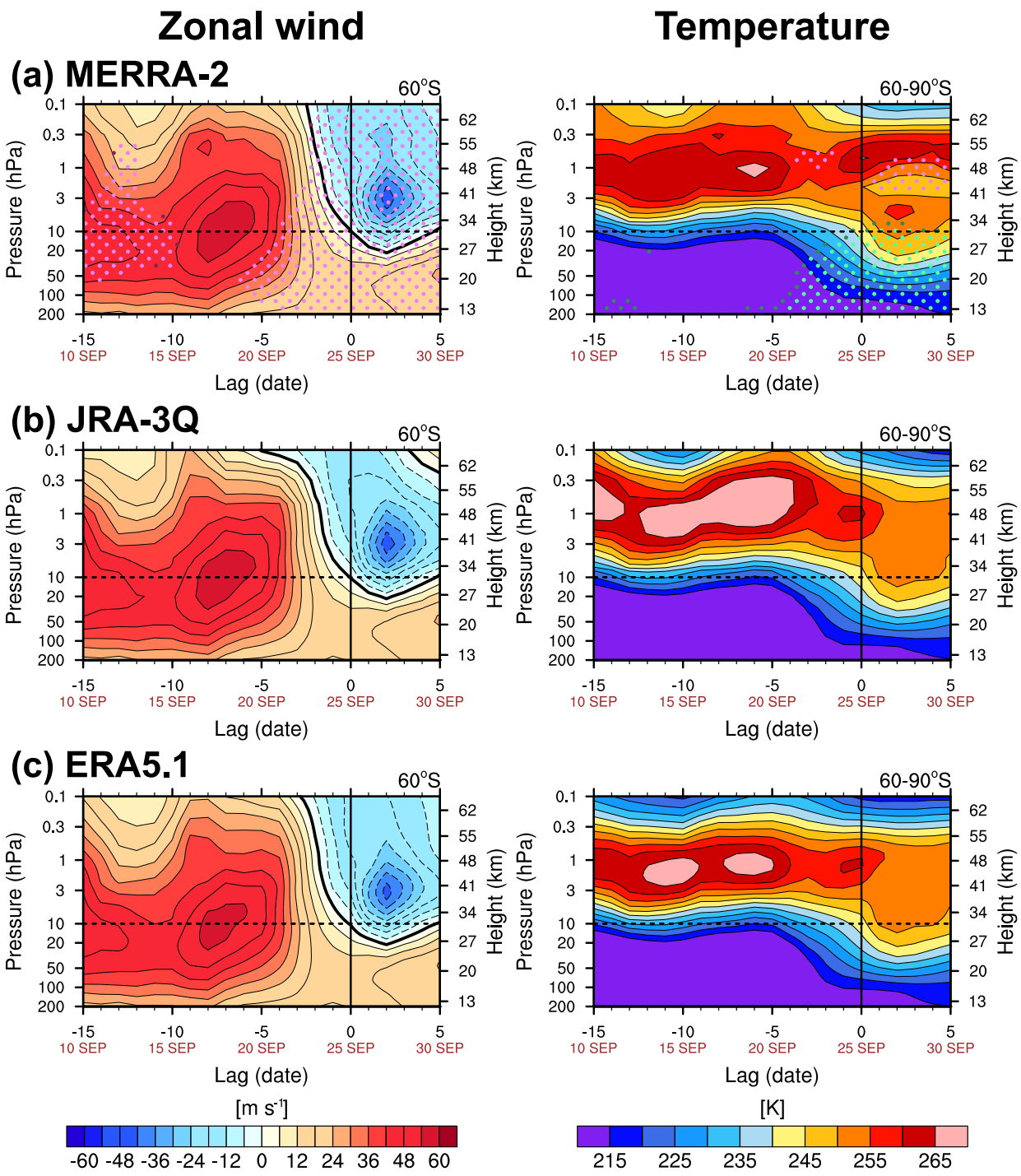

Figure S11. Time–height cross sections of the zonal-mean zonal wind at 60°S (left) and polar cap temperature averaged over 60–90°S (right) revealed in (a) MERRA-2, (b) JRA-3Q, and (c) ERA5.1.

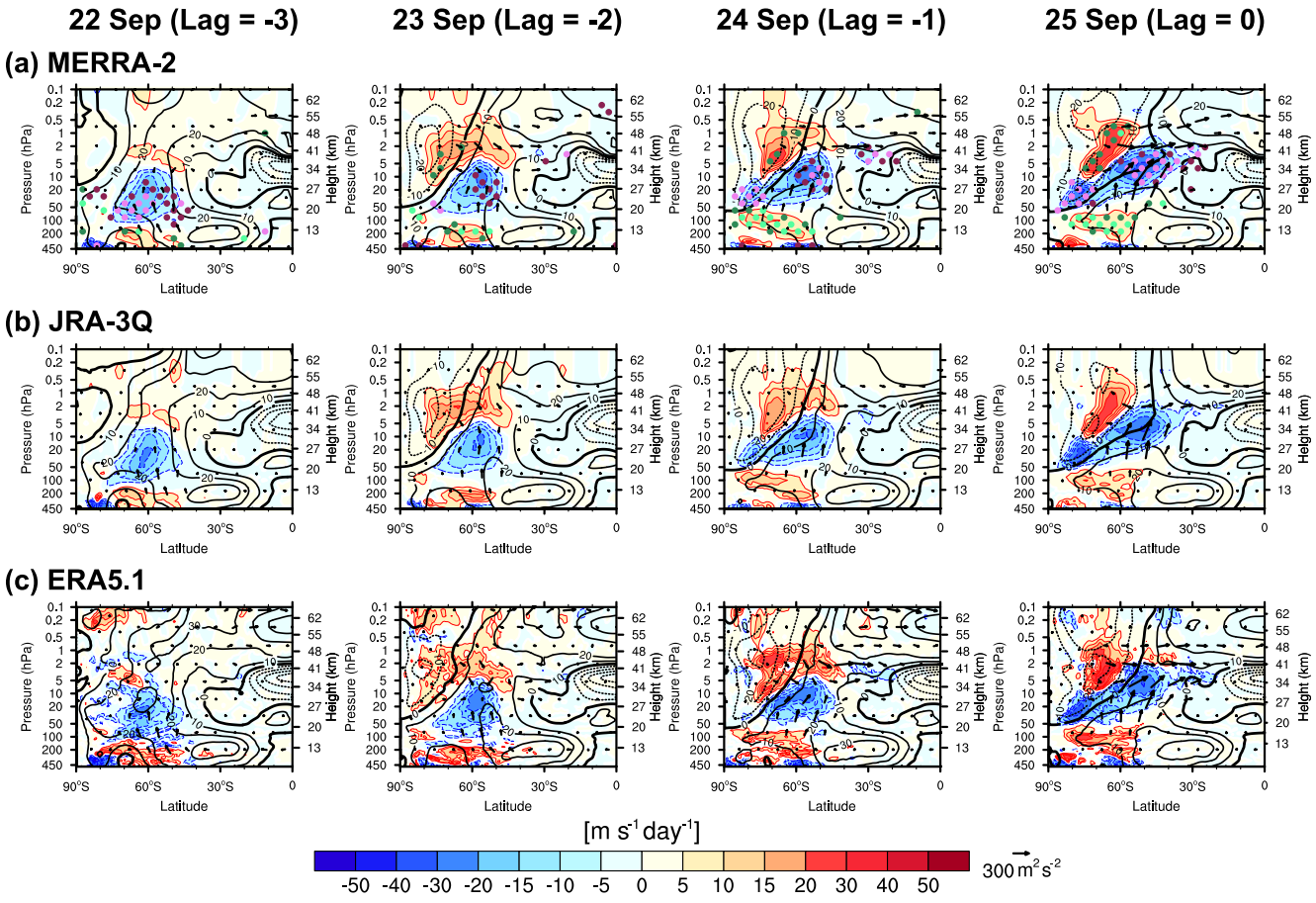

97

98 **Figure S12.** Latitude–height cross sections of the EP-flux (vectors) overlaid on EPFD (shading) for PW2 revealed in (a)
99 MERRA-2, (b) JRA-3Q, and (c) ERA5.1.

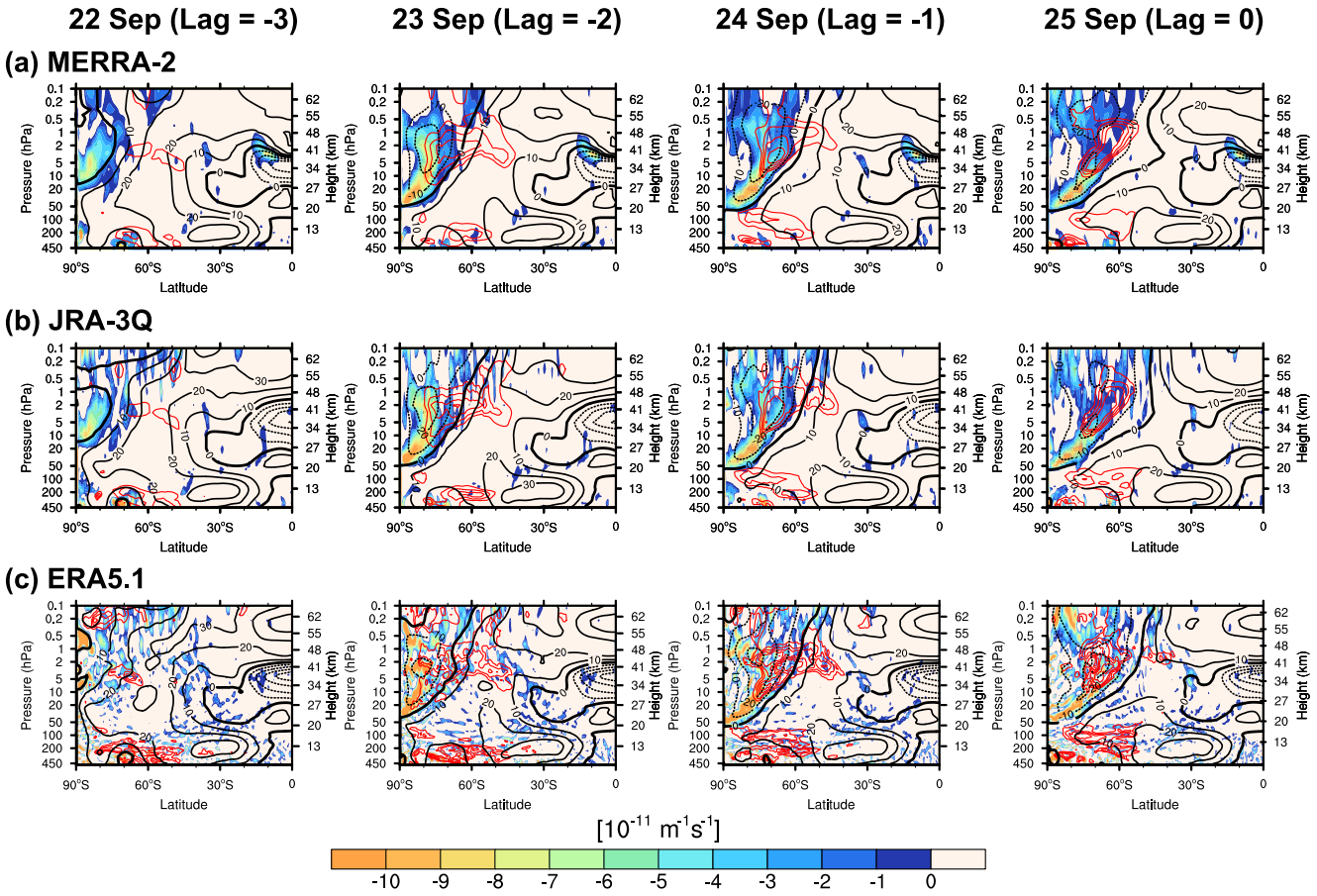

100

101 **Figure S13.** Negative $\bar{q}_y$ (colors) overlaid with the positive EPFD of PW2 (red contours) revealed in (a) MERRA-2, (b)
102 JRA-3Q, and (c) ERA5.1.